

POROSITY-VISCOSITY RELATIONSHIPS DURING COMPACTION OF PUMICE

by

DANIEL GAINER

A THESIS SUBMITTED IN PARTIAL FULFILLMENT OF
THE REQUIREMENTS FOR THE DEGREE OF

BACHELOR OF SCIENCE (MAJOR)

in

THE FACULTY OF SCIENCE

(Geology)

This thesis conforms to the required standard

.....

Dr. Kelly Russell

THE UNIVERSITY OF BRITISH COLUMBIA

(Vancouver)

MARCH 2013

© Daniel Gainer, 2013

Abstract

During compaction of pyroclastic material, strain is mainly accommodated by volume reduction from the closing of pore space. At temperatures above the materials softening point, this deformation is achieved through viscous relaxation. The effective viscosity of the material increases with loss of porosity and increased viscosity can lead to brittle deformation. Here, high temperature experiments are conducted on pumice cores of diameter 4 cm and length 8 cm, sampled from Mount Meager's Pebble Creek Formation using the Volcanic Deformation Rig in the Centre for Experimental Study of the Lithosphere (CESL) at the University of British Columbia. Cores were deformed at 875 °C under a constant displacement rate of 2.78×10^{-4} or at constant loads of 1334 N and 3559 N. Initial and final porosities were measured for each core. The acoustic emissions of brittle deformation were measured with an Acoustic Emission System (PCI-2 AE) where high acoustics indicated fracturing from brittle deformation.

Samples showed a strain dependent rheology where the effective viscosity (η_e) increased with increased strain and reduced porosity until viscous deformation was replaced by viscous and brittle deformation. Results show that at this point of viscous-brittle deformation, the stress required to continue straining the material at the same rate increases exponentially. With a constant applied stress, the strain rate will rapidly decrease across this point. At 875 °C $\text{Log}_{10}(\eta_e)$ increases linearly with porosity loss to a point of zero porosity between $10^{11.5}$ to $10^{14.5}$ Pa s. This relationship is important in the welding of ignimbrites and for volcanic recharge, as pyroclastic material can seal a volcanic conduit. The porosity will affect the materials permeability, which will dictate its ability to either effusively release gases or build up pressure leading to an explosive eruption.

Table of Contents

Cover Page.....	i
Abstract.....	ii
Table of Contents.....	iii
List of Figures.....	v
List of Tables	vi
List of Symbols.....	vii
Acknowledgements.....	viii
Chapter 1: Introduction.....	1
Chapter 2: Background.....	3
2.1 Geological Background: Mount Meager Volcanic Complex	3
Chapter 3: Materials	4
3.1 Macroscopic Description	4
3.2 Pumice Sample Preparation	4
3.3 Density and Porosity	6
Chapter 4: Methodology	8
4.1 Volcanic Deformation Rig (VDR).....	8
4.1.1 Experimental Apparatus	8
4.1.2 Sample Assembly	8
4.1.3 Furnace Assembly	9
4.1.4 Data Output	11
4.2 Acoustic Emissions	12
4.2.1 Device Assembly.....	12
4.2.2 Data Output	13
4.3 Eliminating the Effect of Bulging.....	16
Chapter 5: Experimental Methodology	19
5.1 Preliminary Testing to Determine Temperature of Experiments.....	19
5.2 Constant Displacement Experiments:	22
5.3 Constant Load Experiments:.....	22
5.4 3-D Scanning	23

Chapter 6: Results.....	25
6.1 Data Treatment.....	25
6.2 Mechanical Data	26
6.2.1 Constant Displacement.....	26
6.2.2 Constant Load.....	28
Chapter 7: Data Analysis	32
7.1 Rheological Data.....	32
7.1.1 Constant Strain Rate	32
7.1.2 Constant Stress	34
7.2 Effective Viscosity.....	36
7.3 Effective Viscosity and Porosity.....	37
Chapter 8: Implications.....	39
8.1 Welding of Ignimbrites	39
8.2 Volcanic Recharge	39
Chapter 9: Conclusion	39
References.....	41

List of Figures

FIGURE 1. VOLCANIC DEFORMATION RIG SCHEMATIC.	10
FIGURE 2. FURNACE ASSEMBLY	11
FIGURE 3. VDR DATA MONITORING.....	12
FIGURE 4. AE ASSEMBLY	13
FIGURE 5. ACOUSTIC WAVEFORM SCHEMATIC	15
FIGURE 6: ENERGY OF ACOUSTIC EMISSIONS	16
FIGURE 7. ALUMINA JACKET AND PUMICE CORE.....	17
FIGURE 8. TWO CORES DEFORMED TO 30% STRAIN.....	18
FIGURE 9. SAMPLE CORES OF PUMICE COOKED IN A FURNACE.....	20
FIGURE 10.TEMPERATURE DETERMINATION DATA.....	21
FIGURE 11. NEXTENGINE™ 3-D SCANNER	23
FIGURE 12. 3-D SCAN DATA OUTPUT	24
FIGURE 13. CONSTANT DISPLACEMENT MECHANICAL DATA	27
FIGURE 14. CONSTANT LOAD MECHANICAL DATA.....	29
FIGURE 15. DEFORMED PUMICE CORES	30
FIGURE 16. CONSTANT DISPLACEMENT RHEOLOGICAL DATA.....	33
FIGURE 17. CONSTANT LOAD EXPERIMENTS RHEOLOGICAL DATA	35
FIGURE 18. EFFECTIVE VISCOSITY AND STRAIN.....	36
FIGURE 19. EFFECTIVE VISCOSITY AND POROSITY	37
FIGURE 20. CHANGES IN EFFECTIVE VISCOSITY AND POROSITY.....	38

List of Tables

TABLE 1. PHYSICAL MEASUREMENTS OF THREE PUMICE CORES.	5
TABLE 2. DENSITY AND POROSITY MEASUREMENTS.	7
TABLE 3. EXPERIMENTAL CONDITIONS	26
TABLE 4. PHYSICAL PROPERTIES OF CORES FOR A) FINAL , B) CHANGE FROM INITIAL TO FINAL..	31
TABLE 5. INITIAL AND FINAL EFFECTIVE VISCOSITIES.	38

List of Symbols

MMVC	Mount Meager Volcanic Complex
L	Length (cm)
V_T	Total volume (cm ³)
V_{I+R}	Volume of rock and isolated pore space (cm ³)
ρ_B	Bulk density (g/cm ³)
ρ_R	Rock density (g/cm ³)
ρ_S	Skeletal density
Φ_T	Total porosity
Φ_C	Connected porosity
Φ_I	Isolated porosity
VDR	Volcanic Deformation Rig
LVDT	Linear variable differential transformer
PCI-2 AE	Peripheral Component Interconnect-2 Acoustic Emission System
AE	Acoustic emission
\int	Integral
V	Voltage (V)
V_p	Peak signal voltage (μV)
T	Temperature (°C)
T_g	Glass transition temperature (°C)
~	Approximately
TIN	Triangulated irregular network
σ	Stress (MPa)
π	Pi (number)
r	Radius (m)
ε	Strain
Δl	Change in length (cm)
l	Original length (cm)
t	Time (s)
Δt	Change in time (s)
$\dot{\varepsilon}$	Strain rate s ⁻¹
η_e	Effective viscosity (Pa s)
Φ_0	Initial porosity
Φ_f	Final porosity

Acknowledgements

I would like to thank Dr. Kelly Russell for the supervision, guidance and support throughout the thesis process. As well as taking me on as a student and for inspiring me to research volcanic processes with his volcanology course.

Thank you to Stephan Kolzenburg for training me on the Volcanic Deformation Rig and AE, ordering my ceramic jackets, helping me to design an experimental method, troubleshooting with me, and for the guidance and inspiration throughout the experimental process.

Also in the lab, I would like to thank Amy Ryan for all of her help and support during my experiments and for her final edits, Michelle Campbell for training me on the Nextengine™ 3-D Scanner and for using the Matlab™ code to find the volumes of my cores and James Wells for sampling the pumice, setting up the water line on the VDR, training me on the automated saw, and for the wisdom of his own honors thesis experience.

In addition I want give a special thanks to Jörn Unger in the machine shop for manufacturing my ceramic piston and ceramic spacers. As well as grinding down the pumice cores to appropriate lengths, for his support with using the machinery in the cut room, and for machining parts for the new VDR water line.

I would also like to thank the Ronald C. Wells Scholarship Fund for the \$500 dollar scholarship and the Department of Earth, Ocean and Atmospheric Science for their financial support, and Mary Lou Bevier who instructed the thesis seminar, providing formatting instructions, edits and support.

Thank you also to Darcy Baker for encouraging me to write an honors thesis even though I was only enrolled in the major program.

Finally I would like to thank my parents for their support and encouragement throughout my degree.

Chapter 1: Introduction

All magmas vesiculate at the surface due to the exsolution of volatiles (Walsh and Saar, 2008). This degassing can create highly porous volcanic material. Porosity is linked to permeability, which allows for fluid escape in volcanic conduits and reduces the likelihood that over-pressurization, will cause explosive eruptions. The potential for fluid pressure build up and explosive behavior in a volcanic conduit increases if low porosity material undergoes compaction and welding (Kennedy et al., 2005). Hot fragmental material can sinter and compact in a volcanic conduit on a timescale of hours, and reduce the permeability pathway (Quane et al., 2009). Sintering occurs rapidly at high temperature and can be decoupled from the cooling history. Therefore, when analyzing compaction, the initially fragmented material can be assumed to be consolidated for the entire cooling process (Quane et al., 2009).

Compaction processes also control the welding of pyroclastic density current deposits such as ignimbrites. These deposits are comprised of ash, pumice and lithic fragments with void space both between clasts, and in the pores space of vesicular material (Streck and Grunder, 1995). Quane et al. (2004) modeled this compaction using cores of pyroclastic material and an experimental apparatus to apply an effective stress at temperature. Unconfined cores of highly porous pyroclastic material placed under an effective stress at high temperature undergo shortening. Previous experiments have shown both that shortening in unconfined cores is mainly accommodated by loss of porosity (with minimal bulging), and that the effective viscosity of the material at high temperatures increases with a loss of porosity (Quane et al., 2009).

The purpose of this thesis is to constrain this relationship between the loss of porosity and the effective viscosity of volcanic rocks undergoing viscous deformation. It is important to assess this because the effective viscosity will control the fragmentation of the material. The degree of fragmentation and porosity both contribute to the permeability which will determine the potential for effusive degassing and volcanic recharge.

This study consists of high temperature compaction experiments on cores of Mount Meager pumice at constant loads and constant displacement rate using the Volcanic

Deformation Rig. The porosity of deformed and undeformed cores are determined by helium pycnometry. The style of deformation (viscous or brittle) is determined by monitoring acoustic emissions. This produces results showing the relationship between stress, strain, and porosity. The acoustics show the viscosity by which brittle deformation begins at a particular temperature. These results show the relationship between effective viscosity, and porosity of pyroclastic material and the transition between viscous and brittle behavior with changes in porosity and viscosity.

Chapter 2: Background

2.1 Geological Background: Mount Meager Volcanic Complex

The Mount Meager Volcanic Complex (MMVC) is located in Southwestern British Columbia, approximately 150 km north of Vancouver. This calc-alkaline stratovolcano complex is part of the Garibaldi Volcanic Belt, the northernmost end of the Cascade Volcanic Arc (Green et al., 1988; Read, 1990; Sherrod and Smith, 1990). The MMVC is made of a number of partially overlapping volcanoes and consists of overlapping deposits of andesite lava flows, dacite domes and lava flows, pyroclastic and rock avalanche deposits, and peripheral basaltic lava flows and volcaniclastic deposits (Read, 1977a, 1977b). Activity of MMVC extends from 2.2 Ma to its most recent explosive eruption in 2350 BP (Clague et al., 1995; Leonard, 1995; Read, 1977a). This most recent eruption deposited the Pebble Creek Formation (PCF).

The PCF is predominantly dacitic to trachydacitic in composition and its geology is described by various authors (Hickson et al., 1990; Read, 1977a, 1977b, 1990; Stasiuk et al., 1996; and Stewart et al., 2002, 2008). During the subplinian phase of the 2350 BP eruption, a plume 15-17 km in height produced pumiceous pyroclastic fallout deposits totaling $4.2 \times 10^8 \text{ km}^3$ (Andrews et al., 2012; Hickson et al., 1999). These fallout deposits cover slopes of the northeast end of the MMVC. Proximal deposits of this tephra reach a thickness of 80 m while thin (approximately 5 cm thick) distal layers have been identified in Alberta, approximately 500 km to the NE of the vent (Hickson et al., 1999; Nasmith et al., 1967; Westgate and Dreimanis, 1967). These fallout deposits are unconsolidated, well-sorted and clast-supported, and consist of approximately 90% juvenile, angular, white to cream to light gray pumice clasts (1–50 cm in diameter). Large clasts are commonly fractured, and bread crust textures on the surface are common. Approximately 1–5% of the pumice clasts are banded (Hickson et al., 1999; Stasiuk et al. 1996).

There are four main types of accessory lithic clasts present: gray, porphyritic, dacitic, extrusive volcanic clasts (~4 wt.%), most likely sourced from the Plinth Assemblage; pale pink, medium to coarse grained monzogranite clasts (~2 wt. %), most likely sourced from Miocene fall creek stock; various metamorphic and other (non-granitic) plutonic lithologies,

typically oxidized greenstones, fine grained metasediments and diorites (around 1 wt %), sourced from the Triassic Cadwaller Formation; and welded volcanic breccia clasts (0.4 wt %) sourced from vent breccias predating the PCF (Campbell, 2012).

Chapter 3: Materials

3.1 Macroscopic Description

The pumice clasts have a white cream color, unless oxidized, wherein they are pale orange and pink colored. They are comprised of a white glass matrix with ~60-80% visible vesicles. Vesicles range from 1 to 20 mm in diameter and are typically ellipsoidal. There are minor amounts (>1%) of lithic fragments of dacite within the clasts. Some clasts show minor foliation defined by the orientation and shape of vesicles.

3.2 Pumice Sample Preparation

Pumice blocks with a minimum diameter of 200 mm were sampled from Mount Meager's Pebble Creek Formation. Samples were cut to a 130 mm thickness, and 40 mm diameter cores were drilled within the un-oxidized zone of the blocks. Cores containing cavities greater than 10 mm in diameter were discarded, as major cavities could lead to excess strain localization on the remaining glass framework. This could cause uneven deformation during compaction experiments. The remaining cores were ground down to 100 mm lengths to ensure that the top and side surfaces were perpendicular. Cores used in high strain experiments were later ground down to 80 mm lengths to lower the risk of non-coaxial strain during deformation.

The total volume of each core was measured using the average length and diameter of each sample. Ten measurements of diameter and length were made with digital forceps. The

highest and lowest values were dropped and an average was taken using the remaining data. Each core was weighed three times on an analytical balance with the average taken. Table 1 summarizes the volumes and weights of the cores.

Sample		CORE 5	CORE 8	CORE 9
Height (cm)	1	8.034	8.021	8.008
	2	8.004	8	8.032
	3	8.015	7.998	8.024
	4	8	8.001	8.039
	5	8.005	7.998	8.041
	6	8.001	8.001	8.009
	7	8.006	8.001	8.012
	8	8	7.999	8.023
	9	8.035	8.015	8.008
	10	8.019	8.002	8.006
	average	8.0105	8.002125	8.019625
	std dev	0.011576	0.005357	3.381389
Diameter (cm)	1	3.849	3.894	3.855
	2	3.835	3.868	3.851
	3	3.851	3.833	3.843
	4	3.856	3.885	3.842
	5	3.873	3.887	3.849
	6	3.83	3.872	3.846
	7	3.862	3.833	3.838
	8	3.859	3.904	3.856
	9	3.848	3.897	3.831
	10	3.86	3.837	3.841
	average	3.853875	3.871625	3.84575
	std dev	0.011064	0.02468	0.005946
Volume: (cm ³)		93.44257	94.2067	93.15497
Mass (g)	1	63.6181	61.2954	60.07
	2	63.6183	61.2951	60.0697
	3	63.6182	61.2949	60.0699
	average	63.6182	61.29513	60.06987
	std dev	0.000100	0.000252	0.000153

Table 1. Physical measurements of three pumice cores: Ten measurements of height and diameter are taken with digital forceps. The highest and lowest values (displayed in red) are removed and the remaining measurements averaged. Volume is calculated using $V = \text{diameter}/2 * \pi * \text{height}$. Mass is determined by averaging three measurements on an analytical balance.

3.3 Density and Porosity

Density and porosity measurements were calculated using the measured volumes and masses, helium pycnometry, and data from previous literature.

Pumice contains both isolated and connected pores. Isolated pores are sealed off and do not contribute to the permeability of the sample, while connected porosities allow for fluid flow between them and do contribute to the permeability. The isolated and connected porosities are the volumes of these types of pores as a fraction of the total volume measured by pycnometry. Total porosity is a measure of both isolated and connected porosity and is measured by the volume of both of these pores together as a fraction on the total volume. Porosities are determined through density measurements.

Bulk density (ρ_B) is the density of the total core including rock mass, isolated and connected pores. This is derived by the volume (including all pore space) divided by the mass. Skeletal density (ρ_S) is the density of the rock and isolated porosity and is measured using helium pycnometry. The rock density (ρ_R) is taken from Michol et al, 2008 and was measured by finely crushing the pumice into a powder, weighing it and performing helium pycnometry to determine the density of the solid material only (Michol et al, 2008).

These values of density allow for computation of the types of porosity (Φ), total (Φ_T), connected (Φ_C) and isolated (Φ_I) (Michol et al, 2008):

$$\Phi_T = 1 - \rho_B / \rho_R$$

$$\Phi_C = 1 - \rho_B / \rho_S$$

$$\Phi_I = (\rho_B / \rho_S) - (\rho_B / \rho_R)$$

Density computations are summarized in Table 2.

Sample	Mass (g)	L (cm)	V_T (cm ³)	V_{R+I} (cm ³)	ρ_B (g/cm ³)	ρ_R (g/cm ³)	ρ_S (g/cm ³)	Φ_T	Φ_C	Φ_I
5	63.62	8.0105	93.44	34.41	0.68	2.49	1.85	0.73	0.63	0.09
8	61.30	8.002125	94.21	32.77	0.65	2.49	1.87	0.74	0.65	0.09
9	60.07	8.019625	93.15	32.73	0.64	2.49	1.84	0.74	0.65	0.09

Table 2. Density and porosity measurements for three pumice cores where V_T is the total volume determined using digital forceps, V_{I+R} is the volume of rock and isolated pore space using a helium pycnometer, ρ_B is the bulk density, ρ_R is the rock density, ρ_S is the skeletal density, Φ_T is the total porosity, Φ_C is the connected porosity and Φ_I is the isolated porosity.

Chapter 4: Methodology

4.1 Volcanic Deformation Rig (VDR)

Samples were deformed on timescales of hours at high temperature and constant displacement rates or constant loads using the Volcanic Deformation Rig (VDR).

4.1.1 Experimental Apparatus

The base of the VDR is a LoadTrac II loadframe manufactured by Geocomp Corporation. An electronic stepper motor with a speed range from 5×10^{-6} to 2.5×10^{-2} cm/s controls the displacement using a built in linear variable differential transformer (LVDT) displacement transducer with 0.00013 cm resolution. An S-Type load cell attached to a fixed cross arm sits overtop of the sample and measures the load up to 1136 kg with 0.086 kg resolution. Experimental measurements can be collected every 0.01 s (Quane et al., 2004). The sampling period can be adjusted to any larger interval as needed as only 1948 measurements can be recorded in one experiment.

4.1.2 Sample Assembly

The VDR can accommodate samples up to 4.95 cm in diameter and 10 cm in length. Its upper piston is machined from Rescor 960 alumina with a diameter and length of 4.95 cm and 17.75 cm respectively. Alumina is insulating and retains a high compressible strength of 415 MPa at high temperatures (Quane et al., 2004). It is also subject to measureable amounts of thermo-expansion at high temperature. The piston is suspended from the S-Type load cell by a 2.5 cm stainless steel spacer. The lower piston is identical but shorter (10.16 cm) and with a 3 mm diameter hole drilled through the center to allow a K type sheathed thermocouple to be inserted up through the piston and sit 2 cm into a hole drilled in the base of the sample. This piston sits on top of a stainless steel cylinder, notched to accommodate the thermocouple wire (Quane et al., 2004).

4.1.3 Furnace Assembly

A Zircar-type FIH fiber insulated heater tube furnace is attached to the VDR. The tube is 30.5 cm long with an inner and outer diameter of 7.6 cm and 15.25 cm respectively. It sits on a fibre insulated washer with the same diameters overtop of the steel baseplate. A helically wound Fe-Cr-Al alloy resistant wire embedded in the rigid body of refractory fiber acts as a heating element within the tube and has external ports connected to the Fuji PXZ-4 PID temperature controller. A K-type thermocouple connected to the controller is used to monitor and control the temperature of the sample (Quane et al., 2004). The temperature can be raised at variable rates. For these experiments, rates of 2, 4 and 8 °C per minute were used. Additional thermocouples are placed within protective sleeves and inserted into the furnace tube to monitor the internal temperature of the furnace at various places.

The upper piston's steel spacer and lower piston's base plate are wrapped in 0.635 cm diameter copper tube, through which cold tap water is run constantly to keep the components working below a recommended 60 °C. Figure 1 describes the major components of the VDR.

Convection of air can cause a 40-50°C gradient across the furnace. To reduce convection, Cotronics Rescor blanket insulation is wrapped around the interior, top and bottom of the tube to completely fill the space between the sample assembly and furnace walls (Quane et al., 2004). Additional blanket insulation is placed between the base of the tube and furnace washer and around the top of the tube along with Cotronics Rescor rope insulation. Figure 2 shows the partially and fully assembled furnace.

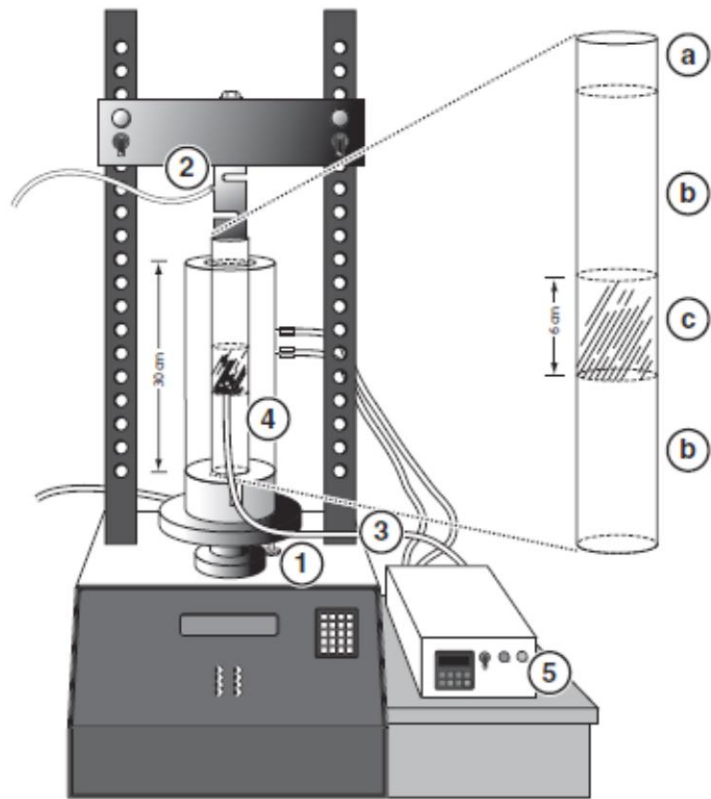


Figure 1. Volcanic Deformation Rig Schematic with a Geocomp Corporation LoadTrac II load frame with linear variable differential transformer (LVDT) displacement transducer (1), a load cell with 1136 kg limit (2), thermocouple (3), fibre-insulated furnace (4), temperature controller (5), steel spacer (a), high temperature ceramic pistons (b), and sample (c) (modified from Quane et al., 2004).

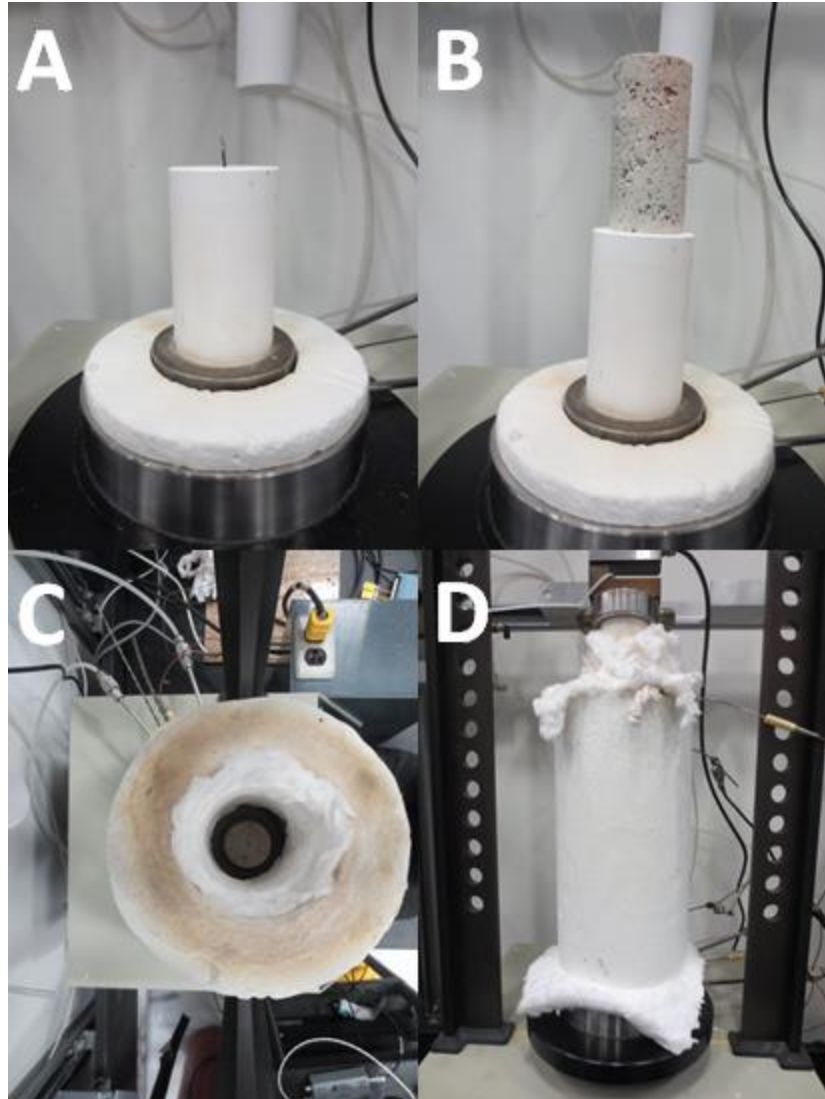


Figure 2. Furnace Assembly: A) Ceramic bottom piston with thermocouple to be inserted in base of the sample. This sits on top of the baseplate along with the fiber insulated washer. B) Set up shown in A now with sample inserted overtop thermocouple. C) View down the top of the furnace which encloses the sample and piston. D) The final assembly with additional Rescore™ blanket and rope, additional thermocouple, and top piston in place.

4.1.4 Data Output

The VDR collects the time (s), load (N) and displacement (cm) for every measurement on an interval defined by the sampling period using Loadtrack software. Temperature (°C) is measured every 2 seconds by the furnace controller and 1 second by the

thermocouple software. Figure 3 shows the data display of time, load, displacement and temperature.

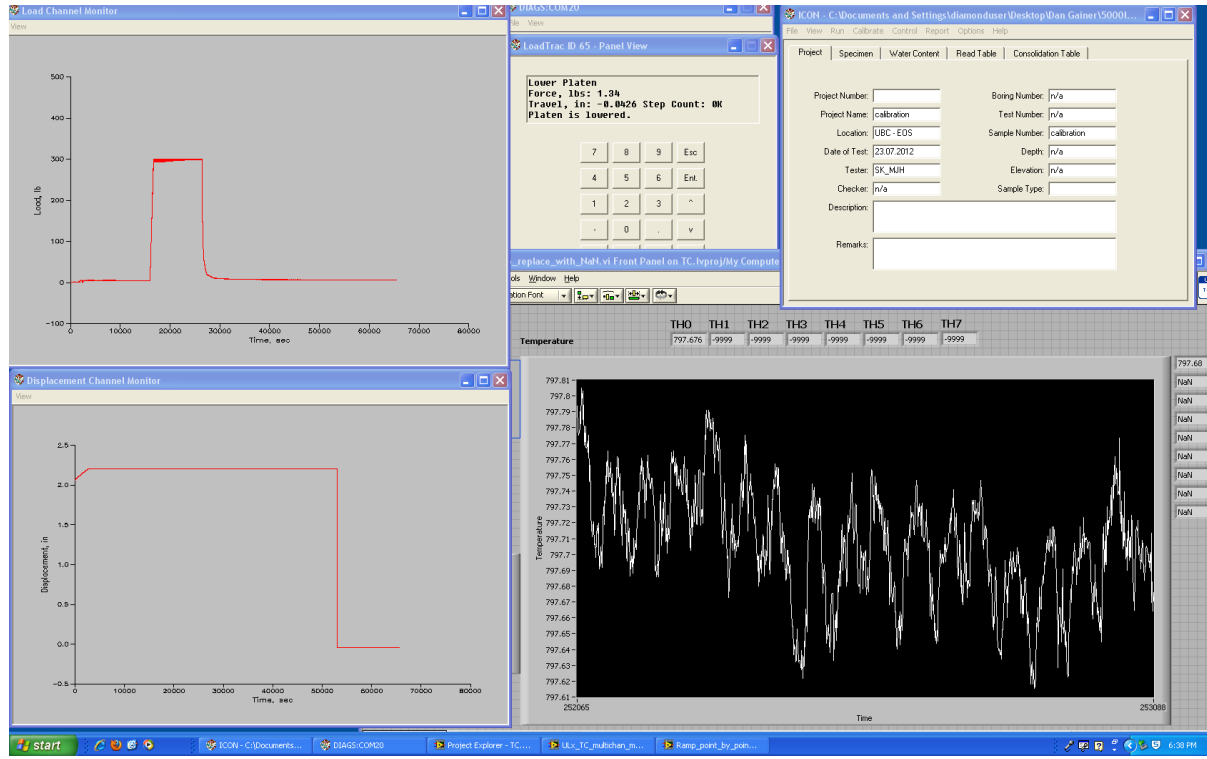


Figure 3. Data monitoring during an experiment on the VDR showing load versus time, displacement versus time and the temperature profile of a thermocouple.

4.2 Acoustic Emissions

A Peripheral Component Interconnect-2 Acoustic Emission System (PCI-2 AE) was used to monitor for acoustics resulting from brittle deformation. This demonstrated where strain was accommodated by brittle and viscous deformation or viscous deformation only.

4.2.1 Device Assembly

The PCI-2 AE is an acoustic emission data acquisition and digital signal processing system. An acoustic emission is an elastic wave generated by the rapid release of energy

[illegible]

4.2.2 Data Output

an acoustic event, duration (the total time of the acoustic event), and amplitude (the largest voltage peak in the AE signal wave). Figure 5 illustrates these parameters as part of a waveform. For the purposes of measuring acoustics of the samples, only energy will be examined as it is analogous to the magnitude of the sound of brittle deformation. Energy is measured in attoJoules (aJ) and is calculated by:

$$\text{Energy} = (\int v^2) / 10\text{k-ohm}$$

where V is the voltage of the signal and 10 k-ohm is the reference resistance of the system. One aJ is equal to 1×10^{-18} Joules (Mistras Group Inc, 2007).

A threshold frequency of 36 dBae was used to eliminate the background noise of the cooling water, and machine noise for low strain experiments. Threshold is defined as the minimum average amplitude that the signal must have to be recorded. The unit dBae measures the amplitude of the wave:

$$\text{dBae} = 20 \log V_p$$

where V_p is the peak signal voltage in microvolts, commonly referred to as the preamplifier input (Mistras Group Inc, 2007). The threshold frequency on a waveform is shown in Figure 5.

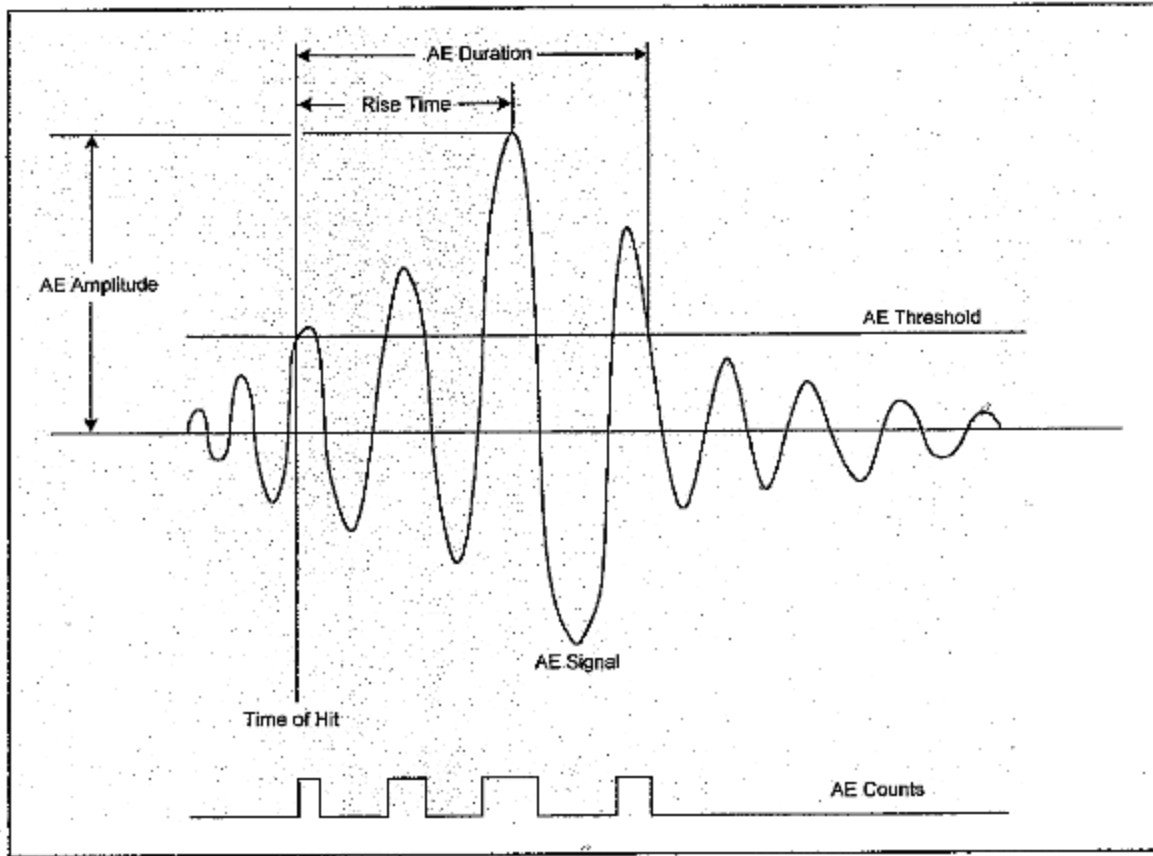


Figure 5. Acoustic waveform schematic showing amplitude, duration, rise, time, count and threshold of the wave (modified from Mistras Group Inc, 2007).

For higher stress experiments, the machine noise exceeded the threshold frequency and needed to be filtered out post experiment. The values of energy were plotted against time in Figure 6. The dense continuous cluster of points with energy below 50 aJ was considered to be background noise. Any acoustic event showing a count of less than 50 aJ was thus considered motor noise and discarded.

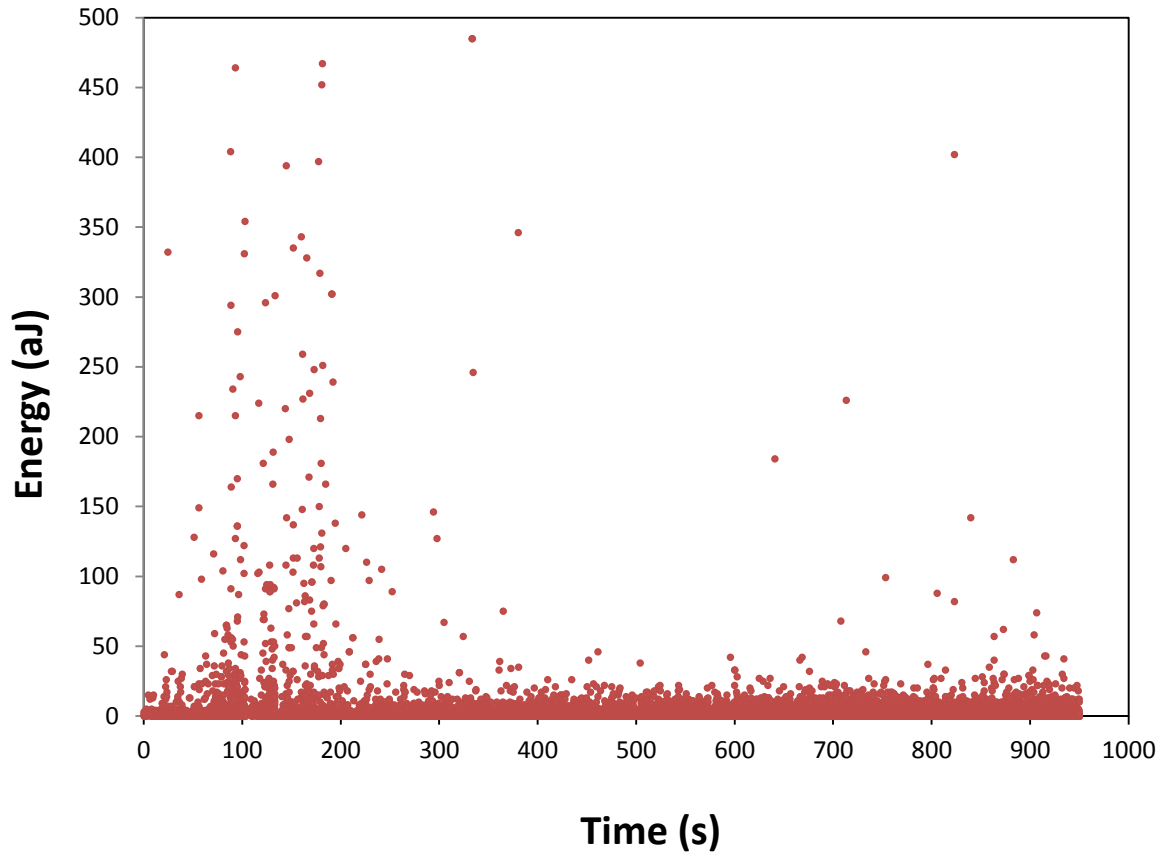


Figure 6: Energy (aJ) of acoustic emissions plotted against time (s) for individual acoustic events. Values below 50 were considered to be engine noise and filtered from final data.

4.3 Eliminating the Effect of Bulging

To ensure that only the effect of volume loss due to closing of pores was measured, the effect of bulging needed to be removed. To prevent bulging, the natural pumice cores were enclosed in ceramic tubes of 97% alumina with an inner diameter of 40 mm (+/- 1mm), an outer diameter of 47 mm (+/- 1mm), and a length of 130 mm (+/- 1mm). Figure 7 shows a core and alumina jacket. Each core was loaded into an alumina tube with alumina spacers placed both above and below the sample. A thermocouple inserted 2 centimeters into the base of the sample through a hole in the bottom spacer controlled the furnace temperature. An additional thermocouple was inserted in the furnace against the sample to monitor the internal temperature of the furnace and to maintain an even temperature gradient.

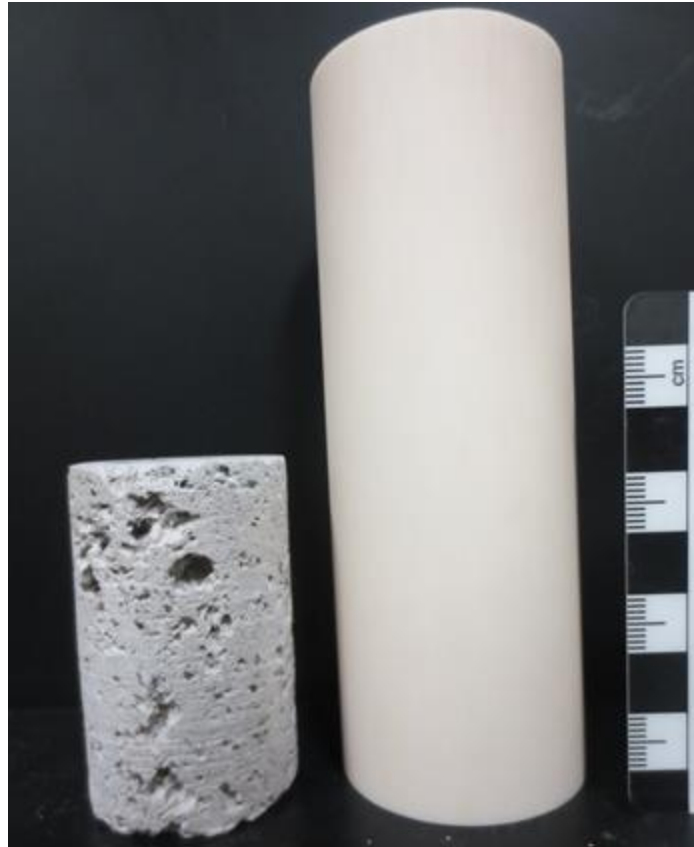


Figure 7. A 130 mm alumina jacket and pumice core.

Initially, each experiment was run once with an alumina jacket and once without to determine the effect of bulging on accommodating shortening. After showing that theunjacketed cores had nearly the same diameter as the jacketed cores, the jackets were no longer used and the effect of bulging was negated. Figure 8 shows two cores deformed at the same level of shortening, one jacketed and one unconfined. The unconfined core showed no major bulging or increase in diameter with some minor localized strain shown by the slight rippled edges. The jacketed core, while oxidizing red due to the alumina, slid free of the jacket upon removal from the assembly after the experiment, showing that its lack of bulging was not controlled by the restraining jacket.



Figure 8. Two cores deformed to 30% strain. The unconfined core shows minor localized strain but no major bulging. The confined core is oxidized red due to the alumina.

Chapter 5: Experimental Methodology

5.1 Preliminary Testing to Determine Temperature of Experiments

In order to reduce the porosity without smashing the rock, the experiments needed to be run at a temperature well above the glass transition temperature (T_g). The glass transition is the melting temperature of the glass in the sample and represents the first appearance of the liquid phase. At this point, a rock may still undergo brittle deformation as most of the rock will be in the solid phase.

The softening point of a rock is a temperature well above the glass transition where enough of the rock has turned to a liquid phase where the rock can deform via viscous relaxation or flow. The softening point was experimentally determined using trial and error.

Test cores were baked in a furnace for 10 hours at 900 °C and 1000 °C and monitored for signs of flow that would indicate the achievement of the softening point temperature. After 2 hours, the 1000 °C core showed no bulging and only minor deformation from flowing; however, the core shriveled up to roughly half its original diameter and was removed. The second core was placed in at 900 °C showed similar shriveling after ten hours.

Shriveling occurs at high temperatures above T_g (B. Kennedy, personal communication, 2013). A temperature above the softening point and below the point of shriveling was necessary to assure viscous deformation and to keep the diameter of the sample constant. The test cores before and after heating are shown in Figure 9.

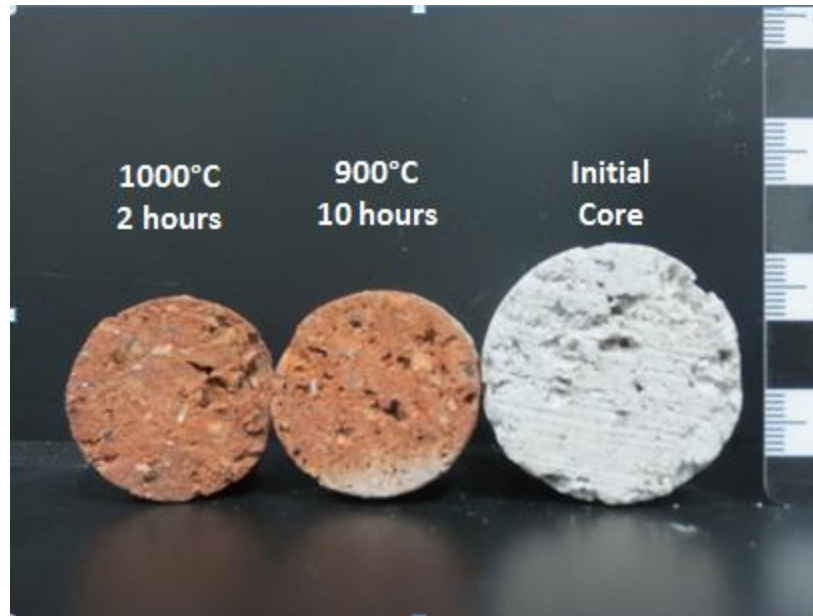


Figure 9. Sample cores of pumice cooked in a furnace at 900 °C and 1000 °C for 10 and 2 hours respectively. Both cores showed significant shriveling relative to the original diameter on the right.

To further constrain the softening point temperature, a core of pumice was deformed at a displacement rate of 1.67×10^{-5} cm/s for 50 minutes with the temperature ramped up from 700 °C to 800 °C. Three thermocouples measured the temperature of the sample. A thermocouple at the base of the sample measured the external temperature of the core and controlled the heating of the furnace, a second thermocouple placed in a hole drilled in the center of the core measured the internal core temperature, and a third thermocouple was placed through the top of the furnace, leaning against the side of the core measured the side surface temperature of the core. The core was held in place under a 22 N load while heated at a rate of 4 degrees per minute up to 700 °C. Stress was applied to the core once all thermocouples read 700 °C.

The AE measured the sound of brittle deformation. The temperature was increased at a steady rate of 2 degrees per minute as the interference pattern of the sound was monitored. High levels of sound indicated cracking and other signs of brittle deformation. Viscous deformation was achieved when the acoustic levels dropped to a constant low value. The thermocouples placed inside the core and leaning against the core displayed a consistent temperature difference of approximately 40 degrees hotter than the controlling thermocouple

at the base of the sample. At 800 °C, measured from the thermocouple within the sample, the load needed to maintain 1.67×10^{-5} cm/s began dropping and the acoustic emissions became quiet showing the softening point for the pumice was reached. To help ensure viscous deformation for the remaining experiments, a temperature 75 °C hotter at 875°C was used. The data is shown in Figure 10.

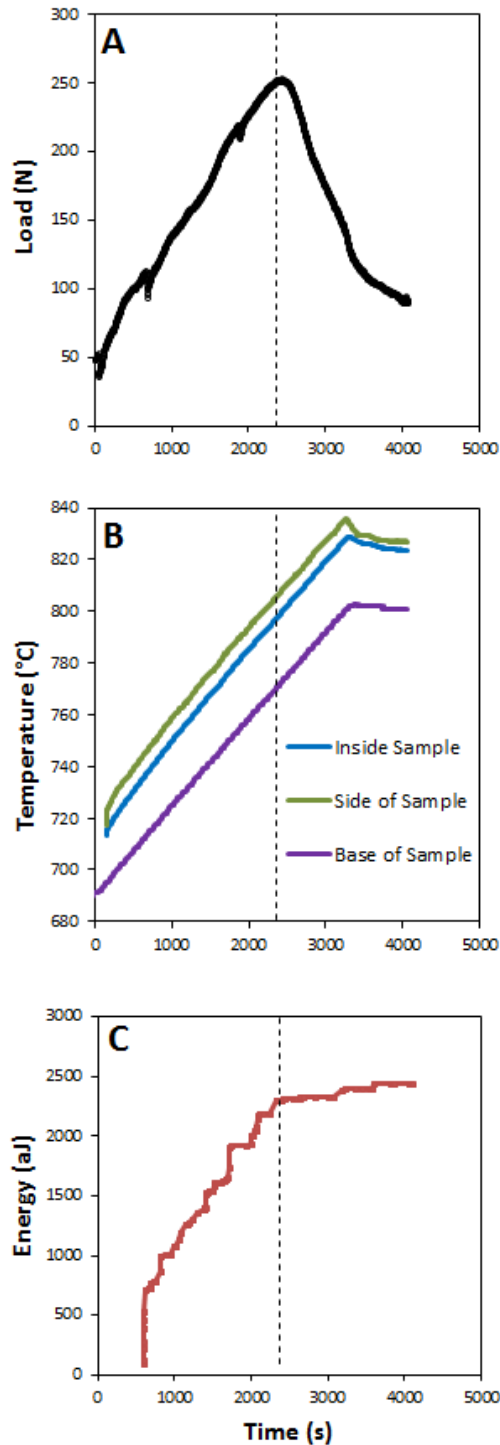


Figure 10. Plots of data from a constant displacement experiment on a 10 cm long core with a displacement rate of 1.67×10^{-5} cm/s. A) Load needed to maintain displacement rate versus time. At ~2300 s the softening point is reached and the load needed to maintain the displacement drops as viscous relaxation occurs. B) Temperature profiles for three thermocouples, one at the base of the sample, one in the center of the sample and one on the exterior of the sample. At 800 °C in the center of the sample the softening point is reached. C) Cumulative energy of acoustic emissions (aJ) of the sample. The steep initial slope shows high energy emissions indicating brittle deformation, the flattening of the graph shows quiet emissions after the softening point is reached and viscous deformation occurs.

5.2 Constant Displacement Experiments:

During a constant displacement rate experiment the base plate of the VDR is moved upwards at a constant rate allowing a linear increase of strain with increasing time. A core was deformed to 50% strain at a constant displacement rate of 2.78×10^{-4} cm/s. The cores were held in place under a constant load of 5 lbs while the temperature ramped up at 8 degrees per minute up to 875 °C. The furnace control thermocouple was placed inside the furnace, up against the side of the core, while a second monitoring thermocouple was placed 2 cm into the base of the core. This reversal of thermocouple setup to the previous experiment was chosen due to the thermal expansion on the ceramic piston at high temperature.

The insulation created by the pumice core made it difficult for the furnace to establish an equilibrium temperature. The furnace would ramp its temperature up and down too highly and over shoot the desired temperature creating a sine wave temperature profile. This temperature profile caused a pattern of thermal expansion and contraction which disrupted the constant displacement data.

A dwell time of 2 hours was used to ensure an even temperature distribution throughout the sample before deformation began. However, the internal temperature of the core was consistently 50 degrees cooler than the furnace temperature. Since both temperatures were above the softening point, and this variation was consistent across all experiments the effect of differential temperature in the sample was negated.

5.3 Constant Load Experiments:

Cores were deformed under constant loads of 1334 N and 3559 N creating stresses of 1.06 MPa and 2.83 MPa respectively. During a constant load experiment the load is increased at a defined load rate to a final load which is then maintained during the rest of the experiment. The load rate must ascend to the final load quick enough as to not cause significant strain on the sample and slow enough as to not cause brittle deformation. A load rate was determined by taking using the initial slope of the curve from the constant displacement experimental data. The load increases at a rate of 111 N in order to begin

deforming the material. At this time the acoustic emissions are quiet, so this rate allowed for relatively quick attainment of the final load without causing brittle deformation. The cores were held in place under constant load of 5 lbs while the temperature ramped up at 8 degrees per minute up to 875 degrees. They had a dwell time of 2 hours before deformation began and were deformed on a time scale of 3 and 4 hours

5.4 3-D Scanning

A NextEngine™ 3-D laser scanner was used to scan the surface of the deformed pumice blocks. Cores were scanned and the data was processed using NextEngine™ ScanStudio HD PRO software. A complete 3-D scan of a pumice core takes 12 minutes to complete, and requires scanning of 12 overlapping segments of the core that are then stitched together. Samples are placed on a rotating plate (shown in Figure 11) which rotates automatically at set increments to allow for successive overlapping scans.

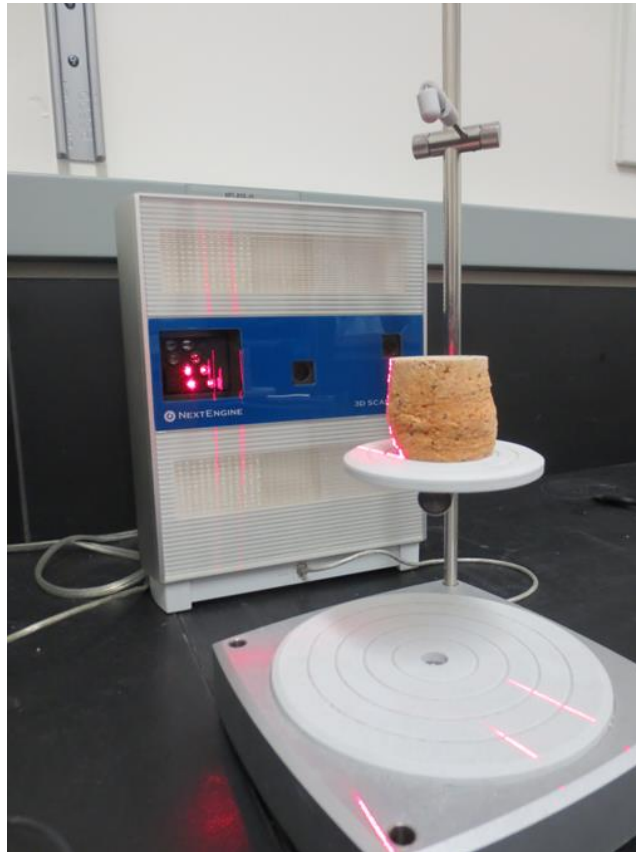


Figure 11. NextEngine™ 3-D Scanner with deformed sample on rotating plate.

These scans create a grid of points in 3 dimensions which are then connected with lines to form a triangulated irregular network (TIN). The 12 scans are stitched together to form one image of the circumference of the core as shown in Figure 12. This image forms a tube shape with no top or bottom and holes where major pores are located. Once the scan is complete, unwanted areas such as the plate are removed using the trim function. This image is then fused to close off any holes in the image to create a 3-D core. As the cores are flat on the top and bottom, these areas were not scanned, and only approximated using the fuse function. This process is demonstrated in Figure 12.

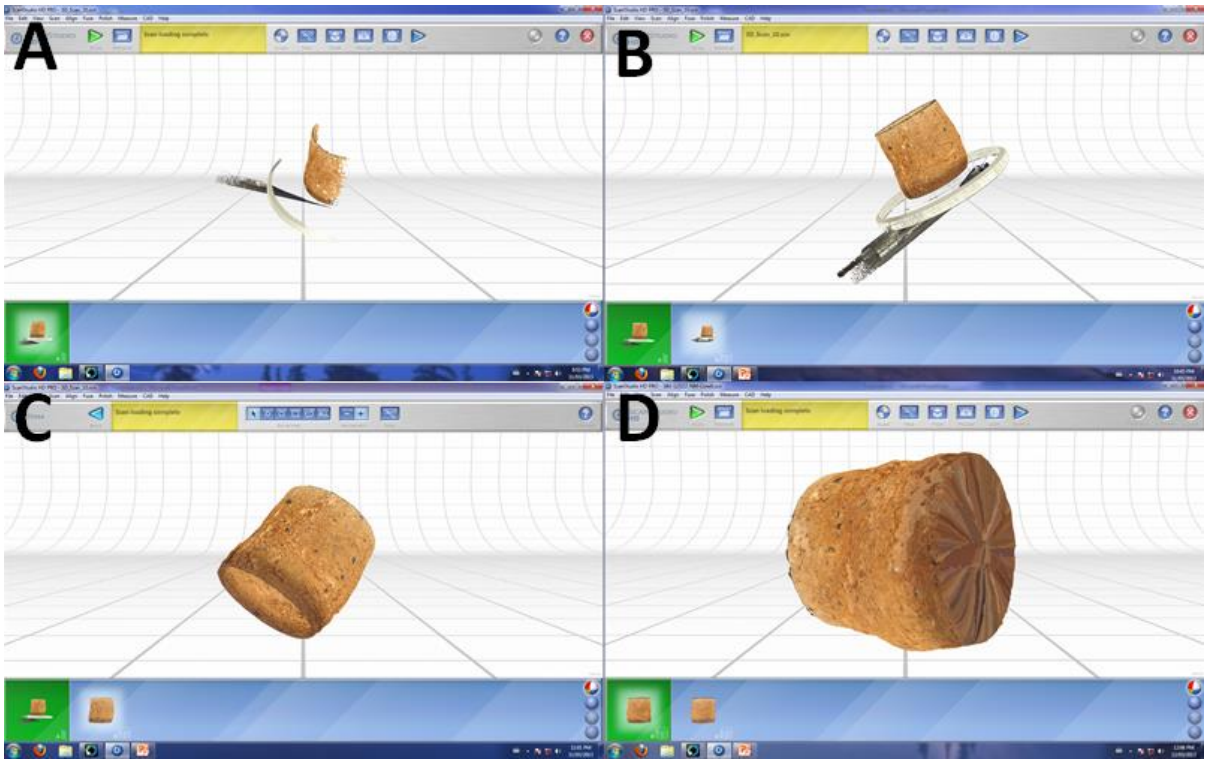


Figure 12. A) A section of core produced during progressive scans and stitching. B) A fully scanned core. C) A core after the excess area have been trimmed off. D) A fused core, where all holes are sealed off to calculate the volume.

The final fused TIN was exported as a .STL file where it was imported into Matlab®. The volumes were computed using the scripts STL_Import.m and SurfaceVolume.m written by Giaccari Luigi.

The initial volumes were computed by measurements of length and diameter using digital forceps and represent the total volume including all pore space. However, these 3-D

rendered volumes exclude pores which contact the surface of the material as seen in Figure 12 and represent a slightly smaller volume. However, this reduction in volume is minimal compared to the volume reduction caused by the deformation.

Chapter 6: Results

6.1 Data Treatment

Under constant temperature experiments, the VDR produces a nearly continuous set of raw measurements of time (s), load (N), and displacement (cm) from which stress (MPa), strain, and strain rate (s^{-1}) can be computed.

Stress (σ) is calculated from:

$$\sigma = \text{load}/\pi r^2$$

where r is the radius of the core.

Strain is calculated as:

$$\varepsilon = \Delta l/l$$

where Δl is the experimental displacement and l is the original length of the core.

Cumulative and incremental strain rate describe strain felt by an object over a time. Cumulative strain rate is the total strain rate up to a particular point in time. Incremental strain rate is the strain rate at one specific point in the data. These are calculated as:

$$\dot{\varepsilon} = (\Delta l/l)/\Delta t$$

where Δt is the time interval. For cumulative strain, Δt will be the total time, Δl will be the total displacement at a point and l will be the original length of the core. For incremental strain, Δt will be the time between the current point and the last measurement, Δl will be the difference in displacement between the current point and last measurement, and l will be the

length of the core at the time of the last measurement (Quane et al, 2008). Table 3 summarizes the experimental conditions and computed data.

Sample	T (°C)	dL/dt (cm/s)	Load (N)	σ (MPa)	ΔL (cm)	ϵ	$\dot{\epsilon}$
5	875	*	1334	1.06	3.35	0.42	*
8	875	2.78E-04	*	*	4.00	0.50	3.47E-05
9	875	*	3559	2.83	4.96	0.62	*

Table 3. Experimental conditions where T is the temperature of the experiment, dL/dt is the displacement rate, σ is the stress, ΔL is the change in length, ϵ is the strain and $\dot{\epsilon}$ is the strain rate.

6.2 Mechanical Data

6.2.1 Constant Displacement

Results are presented in Figure 13 for a constant displacement rate experiment with a rate of 2.8×10^{-4} cm/s and a temperature of 875 °C. An 8 cm long core was compressed at this rate to a final displacement of 4 cm to achieve 50% displacement over a timescale of 4 hours. The load required to maintain the constant displacement rate is measured along with the displacement and time every 8 seconds. The load increases in a smooth line as the displacement increases. Two points are labeled on the line at 1334 N and 3559 N. These points were selected as the loads for two constant load experiments. The deformed core is shown in Figure 15.

Figure 13 also displays two significant load drops at 2224 N and 4448 N. These drops represent the achievement of the final load and end of the experiment. A final load of 2224 N was set on the VDR with the belief that this would be a high enough load to achieve 50 % displacement. However, at a displacement of only 3.23 cm, this load was reached and the VDR began to end the experiment by reducing the load. At this point, the final load was reset to 4448 N and the experiment was continued. Final load was again reached reset to 8896 N to complete of the experiment.

Acoustic emissions are displayed in Figure 13B during the deformation. Here, the cumulative energy in aJ is plotted against time.

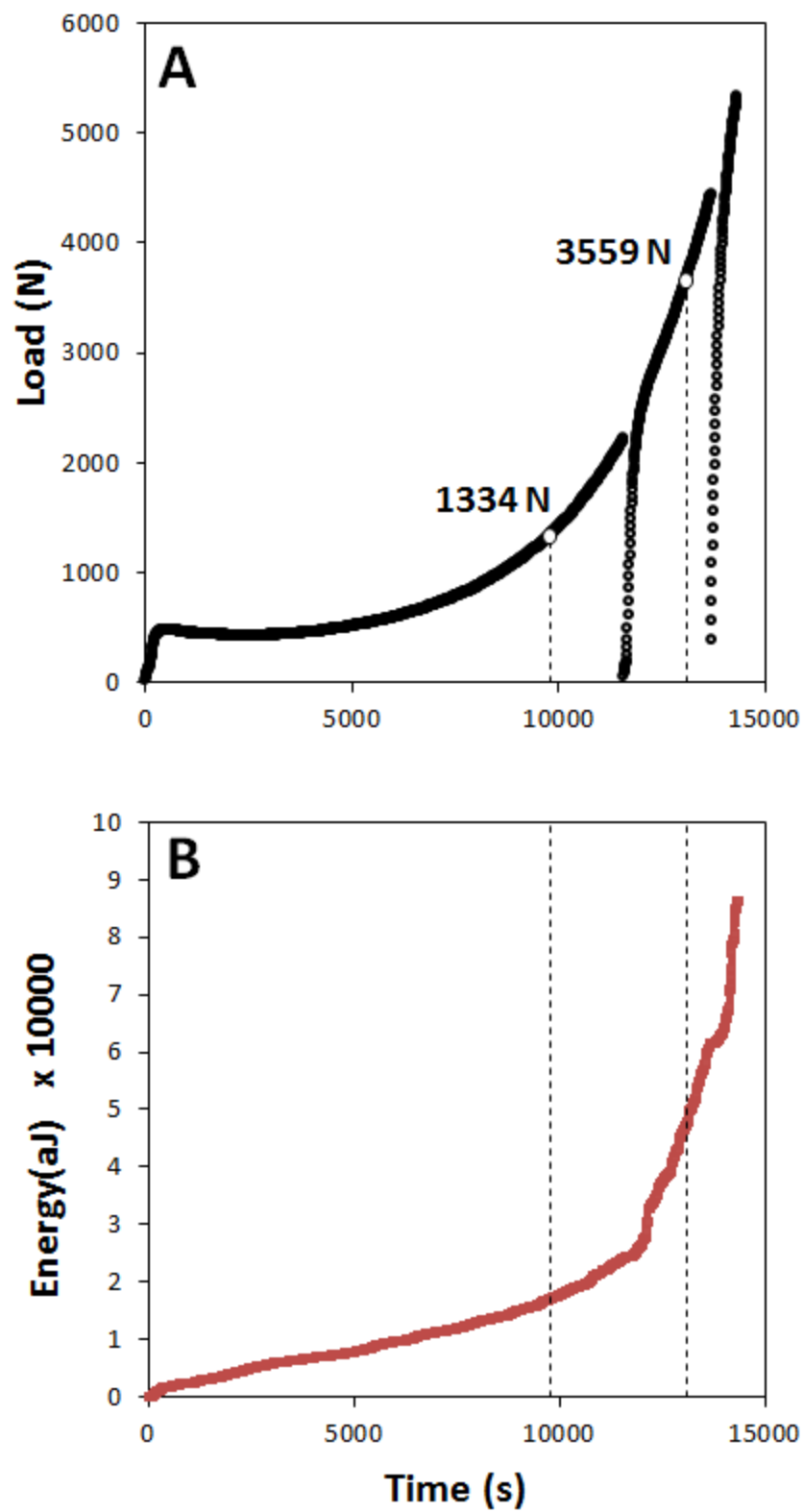


Figure 13. A) Constant displacement experiment mechanical data. Load (N) plotted against time. B) Acoustic energy (aJ) plotted against time.

6.2.2 Constant Load

Results are presented in Figure 14 for two constant load experiments at loads of 1334 N and 3559 N. These loads were chosen from the constant displacement experiment data. Based on the acoustic emissions at these loads, 1334 N sits in the regime of low acoustic emissions whereas 3559 N is in the regime of high acoustic emissions.

The load was increased to the final values at a rate of 1.85 N/s. This rate was chosen based on initial slope of the load curve on the constant displacement experiment. This initial increase in load was fast enough to achieve the final loads before significant viscous relaxation and slow enough to not cause any brittle deformation as shown by the quiet acoustic emissions during the first 250 seconds of the constant displacement experiment.

The vertical lines in Figure 14 show the point at which the final load is reached. Figure 14 also displays the acoustic emissions measured during deformation. Here, the cumulative energy in (aJ) is plotted against time.

Images of the deformed cores from these experiments are shown in Figure 15.

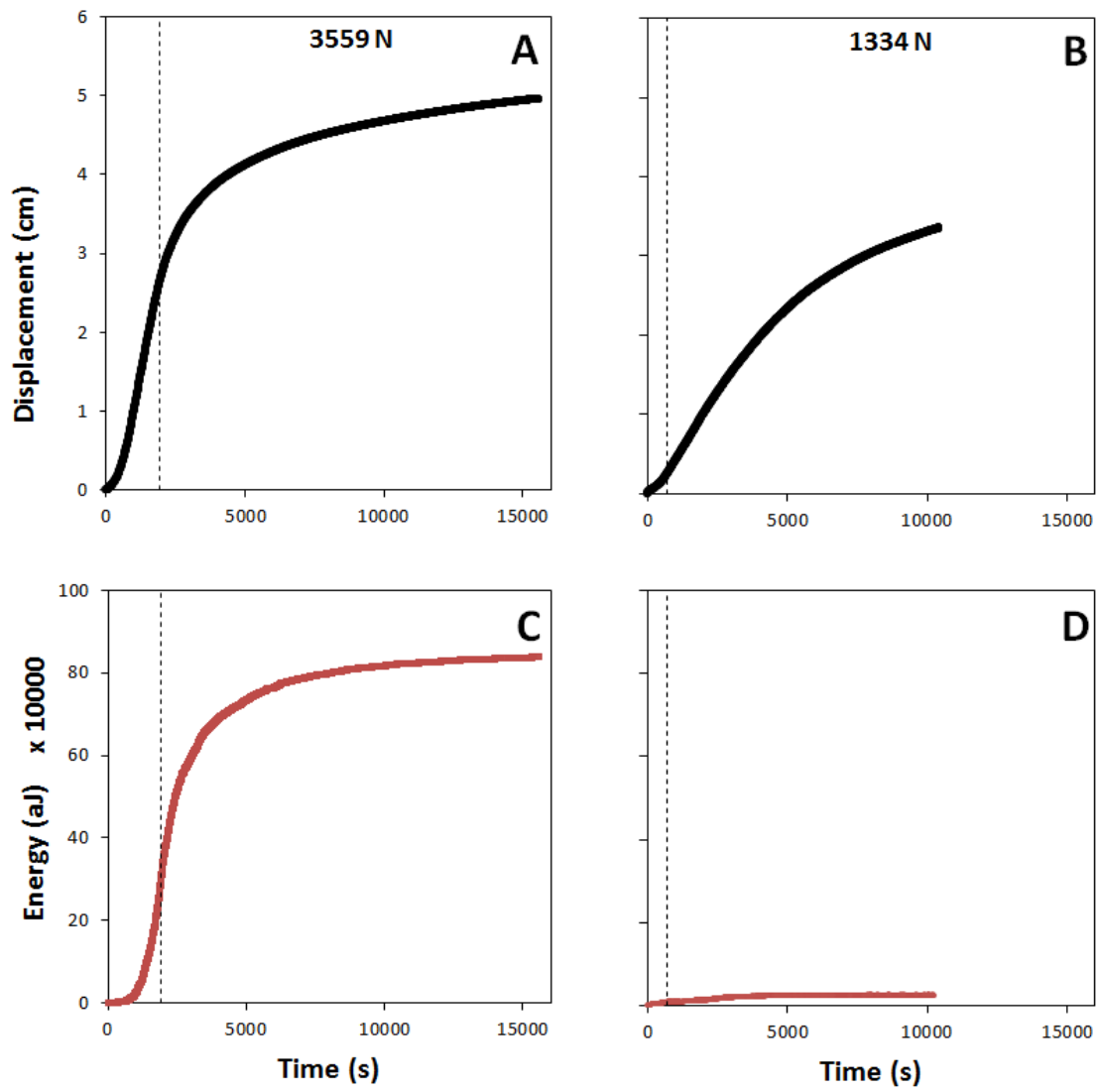


Figure 14. Results of constant load experiments. A) Displacement (cm) against time for 3559 N. B) Displacement (cm) against time for 3559 N. C) Acoustic emissions against time for 3559 N. D) Acoustic emissions against time for 1334 N.



Figure 15. A) 8 cm core before deformation. B) Core deformed to 50% strain in constant displacement. C) and D) Core after 3559 N constant load experiment. E) and F) Core after 1334 N constant load experiment.

A												
Sample	Mass (g)	L (cm)	V_T (cm ³)	V_{R+I} (cm ³)	ρ_B (g/cm ³)	ρ_R (g/cm ³)	ρ_S (g/cm ³)	Φ_T	Φ_C	Φ_I		
5	61.73	4.66	59.32	30.81	1.04	2.49	2.00	0.58	0.48	0.10		
8	59.93	4.00	52.10	28.20	1.15	2.49	2.13	0.54	0.46	0.08		
9	58.79	3.06	40.81	26.68	1.44	2.49	2.20	0.42	0.35	0.08		

B												
Sample	Δ Mass (g)	Δ L (cm)	ΔV_T (cm ³)	ΔV_{R+I} (cm ³)	$\Delta \rho_B$ (g/cm ³)	$\Delta \rho_R$ (g/cm ³)	$\Delta \rho_S$ (g/cm ³)	$\Delta \Phi_T$	$\Delta \Phi_C$	$\Delta \Phi_I$		
5	1.89	3.35	34.13	3.61	0.36	0.00	0.16	0.14	0.15	0.01		
8	1.37	4.00	42.11	4.57	0.50	0.00	0.25	0.20	0.19	0.01		
9	1.28	4.96	52.34	6.05	0.80	0.00	0.37	0.32	0.30	0.02		

Table 4. Physical properties of cores for A) final , B) change from initial to final. L is the length, V_T is the total volume, V_{I+R} is the volume of rock and isolated pore space, ρ_B is the bulk density, ρ_R is the rock density, ρ_S is the skeletal density, Φ_T is the total porosity, Φ_C is the connected porosity and Φ_I is the isolated porosity.

Chapter 7: Data Analysis

7.1 Rheological Data

7.1.1 Constant Strain Rate

Figure 16 shows the stress (σ) in MPa and acoustic emissions (AE) in aJ plotted against strain (ϵ) during the constant displacement experiment. The displacement rate is now shown as a strain rate of $3.5 \times 10^{-5} \text{ s}^{-1}$.

For the first 250 seconds of the experiment, the stress increases at a linear rate of $\sim 2 \text{ N/s}$ to $\sim 500 \text{ N}$. The VDR increases the stress at this rate until it reaches a load high enough to deform the pumice at the desired strain rate. Once this stress is achieved it is roughly maintained over the next 4000 seconds until it begins to increase with increased strain at a nearly exponential rate.

Each time the experiment was restarted, the stress ramped up to the previous final stress before deformation resumed. This demonstrates the implicit relationship between strain and stress. During deformation, the properties of the sample have been altered such that, even with a pause in the experiment it requires at least the same stress or higher to deform the material further as it did to achieve its current level of deformation.

For the first 1200 seconds the acoustics are quiet, with a steady linear trend of shallow slope that represents the background noise of the step motor that drives the piston. However, after 1200 s the energy of the acoustics increases in accordance with exponential increase in stress. This acoustic noise is created by brittle deformation within the sample and this change in slope signifies the boundary between purely viscous deformation and viscous and brittle deformation. This viscous-brittle transition occurs at approximately 40% ϵ .

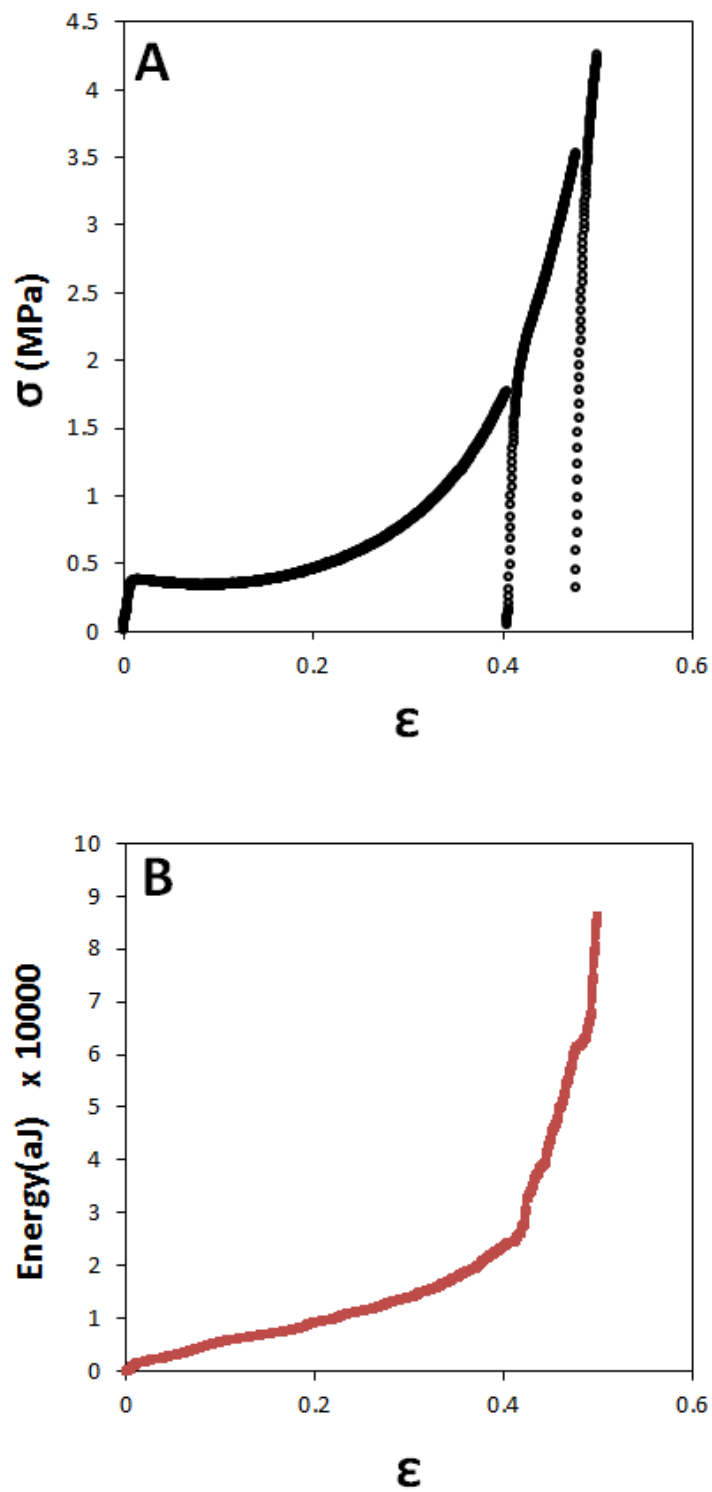


Figure 16. Rheological data of constant displacement experiment. A) Stress (σ) in MPa plotted against strain (ϵ). B) Acoustic energy (aJ) plotted against strain (ϵ).

7.1.2 Constant Stress

Figure 17 presents the constant load experiments in terms of stress and strain. Here, strain (ϵ) and acoustic emissions (AE) in aJ are plotted against time (t) in s for constant stresses of 1.06 MPa and 2.83 MPa which correspond to the loads of 1334 N and 3559 N. The slope of the graph at any point is equal to the strain rate ($\dot{\epsilon}$) at that time.

Both experiments show a similar pattern; an initially high strain rate that decreases as the experiment continues. The 2.83 MPa plot shows a steeper slope which translates to a higher strain rate throughout the experiment than that of the 1.06 MPa experiment. With the higher stress a higher strain rate is achieved as well as a higher overall strain.

The acoustic emissions show that as with the constant displacement experiment, there is a purely viscous regime and a viscous and brittle regime. At 1.06 MPa, the acoustics are quiet without any large jumps in energy indicative of brittle deformation. Therefore 1.06 MPa is not significant enough of a stress at the rate it is applied to initiate brittle deformation. At 2.83 MPa, there is a significant amount of acoustic noise and subsequently brittle deformation that follows a similar trend to the strain curve with high acoustics during high strain rates and low acoustics during low strain rates.

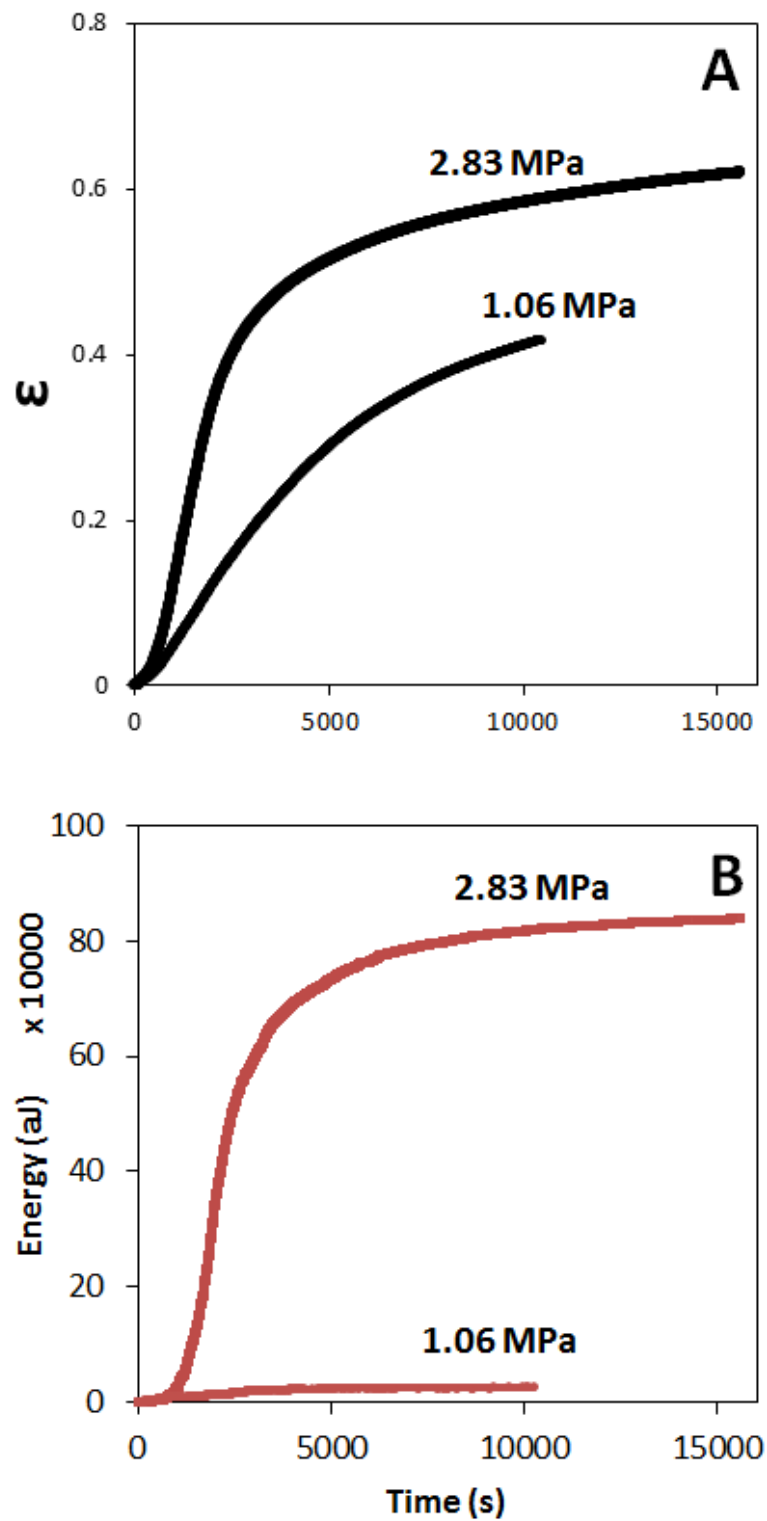


Figure 17. A) Strain plotted against time for 2 constant load experiments with stresses of 1.06 and 2.83 MPa. B) Acoustic energy (aJ) plotted against time.

7.2 Effective Viscosity

Stress and strain can be used to calculate the effective viscosity at each data point during the experiments. Effective viscosity can be calculated by:

$$\eta_e = \sigma / \dot{\epsilon}$$

where σ is the observed stress (MPa), and $\dot{\epsilon}$ is the observed strain rate (s^{-1}) in response to the load stress. The effective viscosity in these experiments is a combination of viscous relaxation and potentially any brittle deformation. Effective viscosity is plotted against strain in Figure 18 for the three experiments. Effective viscosity increases in a non-linear trend with increased strain.

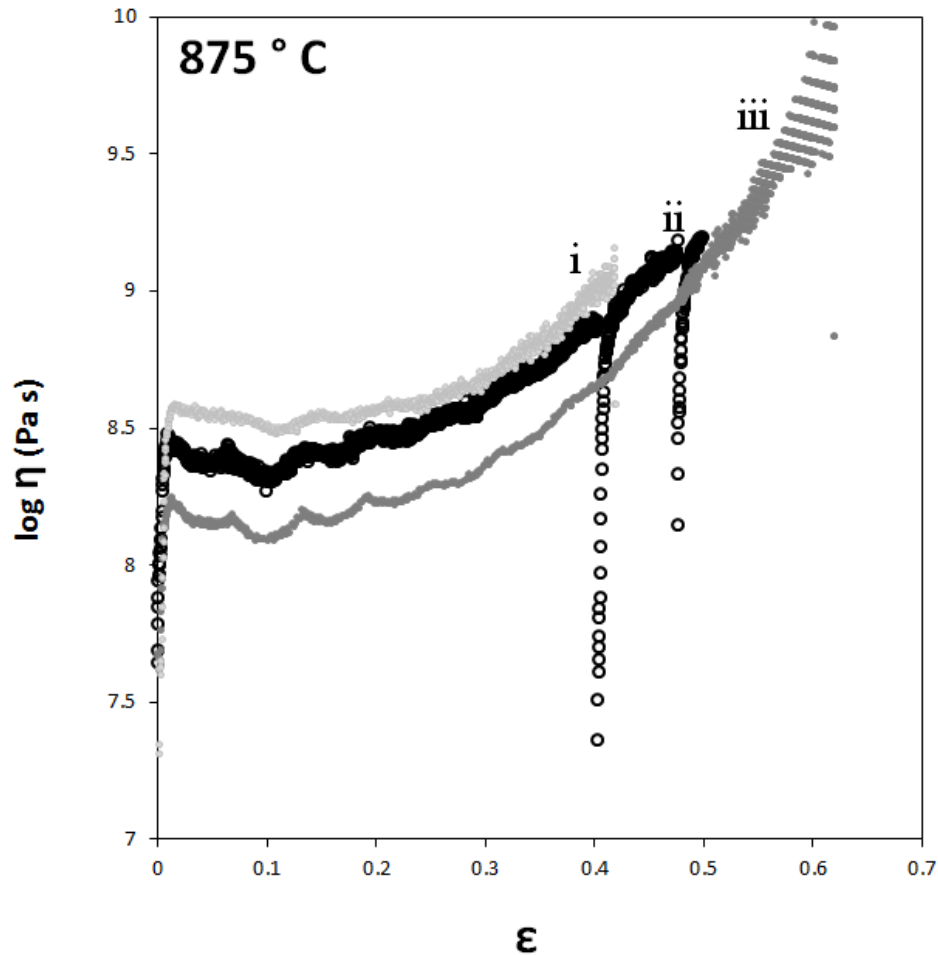


Figure 18. Computed values of Log_{10} of effective viscosity ($\log_{10}\eta_e$) in Pa*s plotted against strain (ϵ) for i) 1334 N of constant load, ii) 50% strain constant displacement rate and iii) 3559 N of constant load. All experiments are at a constant temperature of 875° .

7.3 Effective Viscosity and Porosity

Strain is accommodated in these compaction experiments by volume reduction due to shortening (with minimal accommodation from minor bulging). Volume reduction is in turn accommodated almost exclusively by porosity loss. As the effective viscosity is a function of strain, and strain is manifested via shortening due to loss of porosity, effective viscosity can be shown as a function of porosity. The porosities of the cores were taken before and after deformation were correlated with the initial effective viscosity of the experiment at temperature and the final effective viscosity. Deformation during temperature ramp up or dwell time under the 22 N load used to hold the sample in place was assumed to be minor and negligible in terms of its effect on initial porosity. Any change in porosity that occurred during the cooling period was also negligible. In Figure 19, $\log_{10}(\eta_e)$ is plotted against porosity for the three experiments. Each experiment has a roughly equal initial porosity of ~73% pore space and an initial $\log_{10}(\eta_e)$ of 7.5 to 7.8. Final porosities and effective viscosities vary, though a similar slope is seen between all three experiments. This reflects a reproducible change in viscosity with change in porosity.

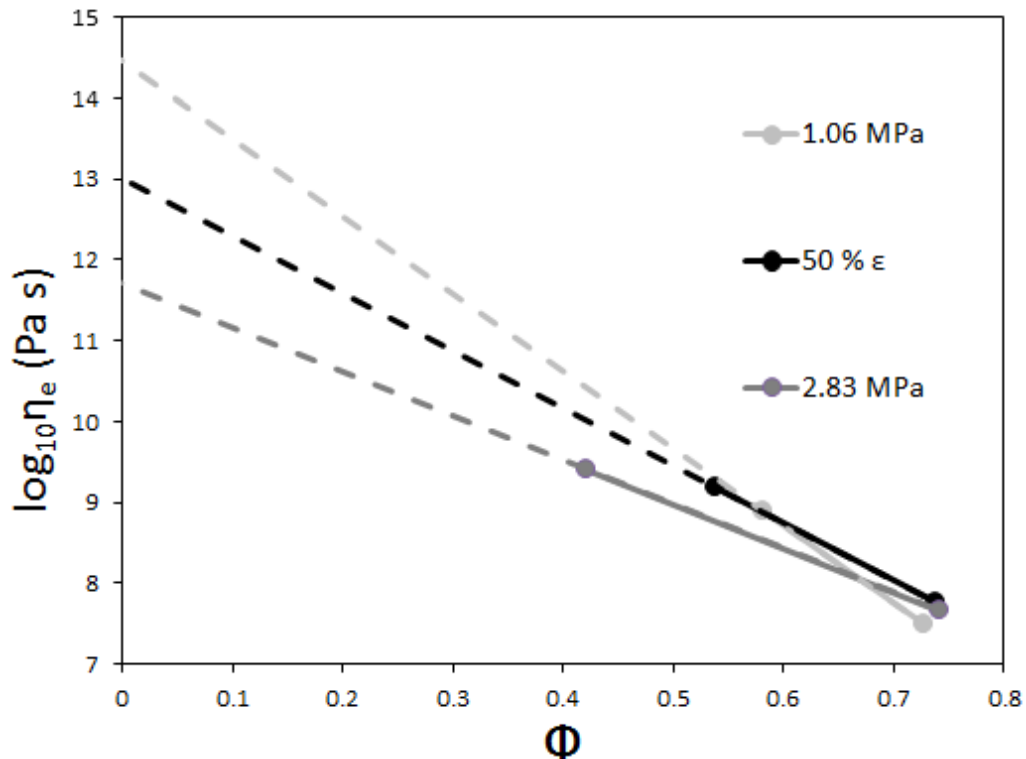


Figure 19. $\log_{10}(\eta_e)$ plotted against porosity for each core the start and finish of the experiment. Each sample has a roughly equal starting porosity and viscosity.

In Figure 19, the effective viscosity at zero porosity is plotted and values of $\text{Log}_{10}(\eta_e)$ at zero porosity range from 1.5 to 14.5. The change in effective viscosity $\log_{10}\eta_{ef}-\log_{10}\eta_{ei}$ is plotted against the change in porosity Φ_f/Φ_o in Figure 20. The three experiments form a positive correlation between loss of porosity and increase in effective viscosity. Under constant displacement experiments, the load stress increases with increasing strain. This shows that the material is strain hardening. This strain hardening is at its highest with the highest amount of strain. This is also true for the constant load experiments since the increased strain causes a reduction in the strain rate with a constant stress applied. Table 5 summarizes the effective viscosity values.

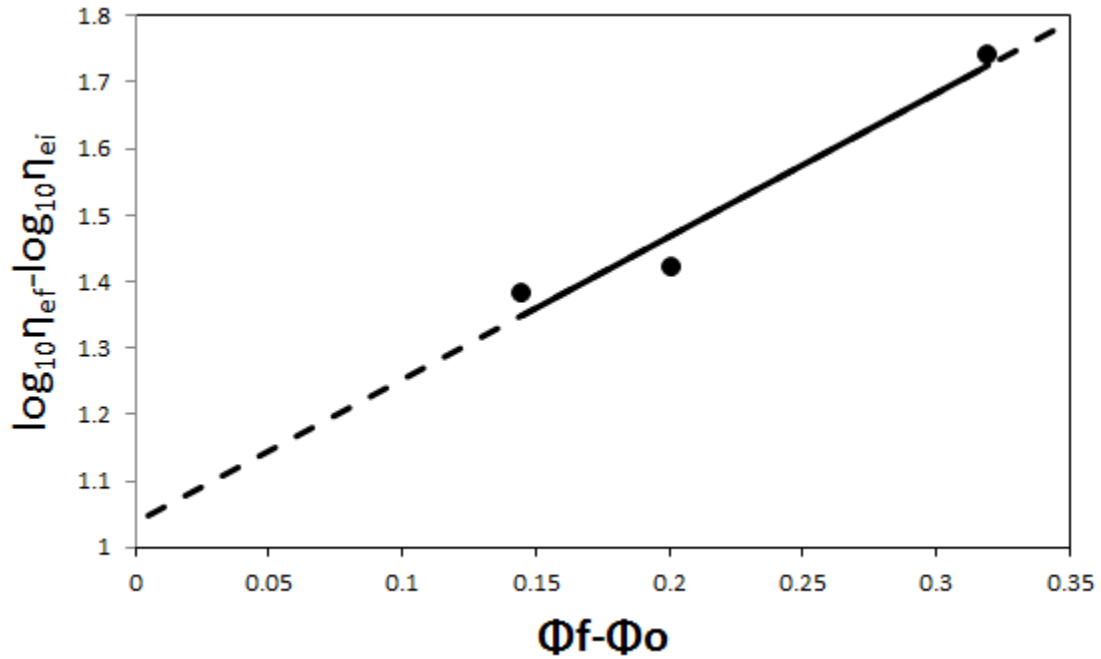


Figure 20. Change in effective viscosity as a function of change in porosity. There is a consistent increase in the change in effective viscosity as the change in porosity increases. A greater loss of porosity creates a greater increase in effective viscosity.

Sample	η_{ei} (Pa s)	η_{ef} (Pa s)	$\log_{10}\eta_{ei}$ (Pa s)	$\log_{10}\eta_{ef}$ (Pa s)	$\log_{10}\eta_{ef}-\log_{10}\eta_{ei}$
5	3.20E+07	7.70E+08	7.51	8.89	1.38
8	5.83E+07	1.54E+09	7.77	9.19	1.42
9	4.55E+07	2.51E+09	7.66	9.40	1.74

Table 5. Initial and final effective viscosities of three experiments, where η_{ei} is the initial effective viscosity, η_{ef} is the final effective viscosity. The \log_{10} is taken to plot linearly against porosity.

Chapter 8: Implications

8.1 Welding of Ignimbrites

A sheet of pyroclastic material varies in thickness during emplacement. Welding occurs rapidly, and on short enough timescales that it can be decoupled from the cooling history. At temperatures well above the glass transition where the material responds viscously to stress, significant loss of porosity can occur with purely viscous deformation. At greater loss in porosity, the effective viscosity increases to a point where brittle deformation occurs. If a constant load is applied to achieve this deformation, the strain rate will decrease significantly at this moment of brittle deformation, as it takes a much higher stress to cause brittle deformation than viscous relaxation.

8.2 Volcanic Recharge

During an explosive volcanic eruption, the column may become filled with pyroclastic material. This material will undergo strain during compaction. The degree to which porosity is lost in the material will dictate its permeability and subsequently its likelihood to create pressure build up in the system. Highly porous material will allow for effusive gas escape while dense material with highly effective viscosities will have lower permeability and can trigger pressure build up.

With high enough effective viscosity, the rock can be weakened by fractures due to brittle deformation, which will increase its fragmentation potential during an eruption.

Chapter 9: Conclusion

Strain during compaction is accommodated by pore collapse and bulging within the core. The effect of bulging can be eliminated by enclosing the core in a jacket, but the effect is small enough that it can be negated even with an unconfined core.

During compaction at temperatures above the softening point, deformation is achieved by viscous relaxation. This can be monitored by measuring acoustic emissions created by brittle deformation in the rock.

The effective viscosity increases during compaction due to loss of porosity. With enough compaction, the effective viscosity reaches a maximum point of purely viscous relaxation. With constant temperature, this point creates brittle deformation that can be determined by monitoring acoustic emissions. Under a constant strain rate of $3.5 \times 10^{-5} \text{ s}^{-1}$ brittle deformation is achieved at 40 % strain. Complete porosity loss at 875 °C yields an effective viscosity of between $10^{11.5}$ to $10^{14.5} \text{ Pa s}$.

This relationship between porosity and effective viscosity will dictate the degree of strain with depth in welded ignimbrites, and the style of deformation associated with this strain. These relationships are also important for understanding the permeability controls on pyroclastic material in volcanic conduits. Porosity will affect the ability for effusive eruptions and significant loss of porosity can lead to pressure build up and explosive eruptions.

References

- Andrews, G.D.M., Russell, J.K., Stewart, M.L., 2012, The rise and fall of a welded pyroclastic dam: the 2,360 BP eruption of Mount Meager, British Columbia, Canada: *Bulletin of Volcanology* In Review.
- Campbell, M., 2012, Thermomechanical milling of lithics in volcanic conduits: (Masters thesis): University of British Columbia.
- Clague, J.J., Evans, S.G., Rampton, V.N., Woodsworth, G.J., 1995, Improved age estimates for the White River and Bridge River tephra, western Canada: *Canadian Journal of Earth Sciences*, v. 32, p. 1172-1179.
- Cui, Y., and Russell, J.K., 1995, Magmatic origins of calc-alkaline intrusions from the Coast Plutonic Complex, southwestern British Columbia: *Canadian Journal of Earth Science* v. 32, p. 1643–1667.
- Green, N.L., Armstrong, R.L., Harakal, J.E., Souther, J.G., Read, P.B., 1988, Eruptive history and KAr geochronology of the Late Cenozoic-Garibaldi Volcanic Belt, southwestern British Columbia: *Geological Society of America Bulletin*, v. 100, p. 563-579.
- Hickson, C.J., Russell, J.K., Stasiuk, M.V., 1999, Volcanology of the 2350 B.P. Eruption of Mount Meager Volcanic Complex, British Columbia, Canada: Implications for Hazards from Eruptions in Topographically Complex Terrain, p. 489-507.
- Kennedy, B., Spieler, O., Scheu, B., Kueppers, U., and Dingwell, D.B., 2005, Conduit implosion during vulcanian eruptions: *Geology*, v. 33, p. 581-584, doi:10.1130/G21488.1.
- Leonard, E.M., 1995, A varve-based calibration of the Bridge River tephra fall: *Canadian Journal of Earth Sciences*, v. 32, p. 2098-2102.
- Michol, K.A., Russell J.K., Andrews G.D.M., 2008, Welded block and ash flow deposits from Mount Meager, British Columbia, Canada: *Journal of Volcanology and Geothermal Research*, v. 169, p. 121-144.
- Mistras Group Inc., 2007, PCI-2 based AE system user's manuel. Princeton Junction, NJ: Physical Acoustics Corporation.
- Nasmith, H., Mathews, W.H., Rouse, G.E., 1967, Bridge River ash and some other recent ash beds in British Columbia: *Canadian Journal of Earth Sciences*, v. 4, p. 163-170.
- Quane, S.L., Russell, J.K., and Kennedy, L.A., 2004, A low-load, high-temperature deformation apparatus for volcanological studies: *American Mineralogist*, v. 89, p. 873–877.

Quane, S.L., and Russell, J.K., 2005b, Welding: Insights from high-temperature analogue experiments: *Journal of Volcanology and Geothermal Research*, v. 142, p. 67–87, doi: 10.1016/j.jvolgeores.2004.10.014.

Quane, S.L., Russell, J.K., and Friedlander, E. A., 2009, Time scales of compaction in volcanic systems: *Geology*, v. 37, p. 471-474, doi: 10/1130/G25625A.1.

Read, P.B., 1977a, Meager Creek volcanic complex, southwestern British Columbia. Report of Activities, Part A: Geological Survey of Canada Paper, v. 77-1A, p. 277-281.

Read, P.B., 1977b, Geology of Meager Creek geothermal area, British Columbia: Geological Survey of Canada Open File 603, Scale 1:20 000.

Read, P.B., 1990, Mount Meager Complex, Garibaldi Belt, Southwestern British Columbia: *Geoscience Canada*, v. 17, p. 167-170.

Russell, J.K., and Quane, S.L., 2005, Rheology of welding: Inversion of field constraints: *Journal of Volcanology and Geothermal Research*, v. 142, p. 173–191, doi: 10.1016/j.jvolgeores.2004.10.017.

Sherrod, D.R., Smith, J.G., 1990, Quaternary Extrusion Rates of the Cascade Range, Northwestern United States and Southern British Columbia: *Journal of Geophysical Research* 95, v. 19, p. 465- 419,474.

Stasiuk, M.V., Russell, J.K., Hickson, C.J., 1996, Distribution, nature, and origins of the 2400 B.P. eruption products of Mount Meager, British Columbia: linkages between magma chemistry and eruption behaviour: *Geological Survey of Canada Bulletin*, p. 486.

Stewart, M.L., Russell, J.K., Hickson, C.J., 2002, Revised stratigraphy of the Pebble Creek Formation, British Columbia: evidence for interplay between volcanism and mountainous terrain.

Streck, M.J., and Grunder, A.L., 1995, Crystallization and welding variations in a widespread ignimbrite sheet; the Rattlesnake Tuff, eastern Oregon, USA: *Bulletin of Volcanology*, v. 57, p. 151–169.

Walsh, S.D.C., and Saar, M.O., 2008, Magma yield stress and permeability: Insights from multiphase percolation theory: *Journal of Volcanology and Geothermal Research*, v. 177, p. 1011–1019, doi: 10.1016/j.jvolgeores.2008.07.009.

Westgate, J.A., Dreimanis, A., 1967, Volcanic ash layers of Recent age at Banff National Park, Alberta, Canada: *Canadian Journal of Earth Sciences*, v. 4, p. 155-161.